

 Open access • Journal Article • DOI:10.1088/0022-3727/44/36/365202

## Time-resolved mass spectroscopic studies of an atmospheric-pressure helium microplasma jet — [Source link](#)

Jun-Seok Oh, Yolanda Aranda-Gonzalvo, James W. Bradley





**Institutions:** University of Liverpool

**Published on:** 14 Sep 2011 - Journal of Physics D (IOP Publishing)

**Topics:** Jet (fluid), Ion, Rise time and Atmospheric pressure

Related papers:

- [Applied Plasma Medicine](#)
- [Mass spectrometric diagnosis of an atmospheric pressure helium microplasma jet](#)
- [Plasma medicine: an introductory review](#)
- [Imaging gas and plasma interactions in the surface-chemical modification of polymers using micro-plasma jets](#)
- [Chemical kinetics and reactive species in atmospheric pressure helium?oxygen plasmas with humid-air impurities](#)

Share this paper:    

View more about this paper here: <https://typeset.io/papers/time-resolved-mass-spectroscopic-studies-of-an-atmospheric-3w36hdhwul>



# Time-resolved mass spectroscopic studies of an atmospheric-pressure helium microplasma jet

Jun-Seok Oh, Yolanda Aranda-Gonzalvo, James W Bradley

## ► To cite this version:

Jun-Seok Oh, Yolanda Aranda-Gonzalvo, James W Bradley. Time-resolved mass spectroscopic studies of an atmospheric-pressure helium microplasma jet. *Journal of Physics D: Applied Physics*, IOP Publishing, 2011, 44 (36), pp.365202. 10.1088/0022-3727/44/36/365202 . hal-00651638

**HAL Id: hal-00651638**

**<https://hal.archives-ouvertes.fr/hal-00651638>**

Submitted on 14 Dec 2011

**HAL** is a multi-disciplinary open access archive for the deposit and dissemination of scientific research documents, whether they are published or not. The documents may come from teaching and research institutions in France or abroad, or from public or private research centers.

L'archive ouverte pluridisciplinaire **HAL**, est destinée au dépôt et à la diffusion de documents scientifiques de niveau recherche, publiés ou non, émanant des établissements d'enseignement et de recherche français ou étrangers, des laboratoires publics ou privés.

# Time-resolved mass spectroscopic studies of an atmospheric-pressure helium microplasma jet

Jun-Seok Oh<sup>a)</sup>, Yolanda Aranda-Gonzalvo<sup>b)</sup> and James W. Bradley<sup>a)c)</sup>

<sup>a)</sup> *Department of Electrical Engineering and Electronics, University of Liverpool, L69 3GJ, Liverpool, UK*

<sup>b)</sup> *Hidden Analytical Ltd., 420 Europa Boulevard Gemini Business Park, WA5 7UN, Warrington, UK*

<sup>c)</sup> Author for correspondence: [j.w.bradley@liv.ac.uk](mailto:j.w.bradley@liv.ac.uk)

## Abstract

Using molecular beam mass spectroscopy, time-resolved measurements of the ionic species in the plasma plume of an atmospheric-pressure helium microplasma jet have been made for a range of excitation frequencies (5, 10 and 25 kHz) and source-instruments orifice distances (1, 7 and 11 mm). Ionic species can only be observed in the visible plasma plume, with the main positive species being  $\text{N}_2^+$  (65.26%) and  $\text{O}_2^+$  (21.11%), and few percentages of  $\text{N}^+$ ,  $\text{O}^+$ ,  $\text{NO}^+$  and  $\text{He}^+$ . For the negative ions, the majority species are  $\text{O}_3^-$  (22.68 %),  $\text{O}_2^-(\text{H}_2\text{O})$  (10.49 %) and a large range of minority species observed namely,  $\text{O}_n^-$ ,  $\text{OH}_n^-$ ,  $(\text{H}_2\text{O})_n^-$ ,  $\text{CO}_n^-$  and clusters,  $\text{O}_m^-(\text{H}_2\text{O})_n$ ,  $(\text{OH})_m^-(\text{H}_2\text{O})_n$ ,  $\text{O}_n^-(\text{CO}_3)$  and  $\text{CO}_3^-(\text{H}_2\text{O})_n$ . The flux of ions created from air species such,  $\text{NO}^+$  and  $\text{O}_3^-$ , are seen to be maximized a distance of several mm from the nozzle, whereas the  $\text{He}^+$  concentration continually decreases with distance from the exit orifice. The time-resolved measurements (time-resolution down to 2  $\mu\text{s}$ ) show positive ions appear twice in one full period of the voltage waveform, correlated directly with positive and negative current peaks. The rise and fall times of the positive ions are typically tens of  $\mu\text{s}$ . In contrast, the appearance of negative ions is correlated only with the negative part of discharge current, with one main peak in the detected ionic flux seen per cycle. The rise time of the negative ions is about 10  $\mu\text{s}$ , independent of mass, however we observed longer decay times from 100 to 150  $\mu\text{s}$  increasing with mass. With increased driving frequency, the time

modulation in the ionic fluxes is reduced, particularly for the negative species that show almost constant fluxes at 25 kHz throughout the cycle. The observations can be understood through a simple picture of the interaction of the He jet and the moist ambient air. The results indicate that the discrete plasma “bullets” and their afterglow tail, that forms the jet, carry an associated positive or negative current depending on the time of their creation in the voltage cycle.

## 1. Introduction

Low-pressure plasma discharges are a useful tool in a number of surface treatment and polymerisation applications, since the plasma can act isotropically on irregular surfaces in large volumes whilst delivering good uniformity on substrates of all sizes [1]. In recent years, however, there has been much interest in developing plasmas on the micro-scale which operate at, or close to atmospheric-pressure [2] to deliver cheap processing solutions with opportunities to functionalise surfaces on the small scale. One candidate plasma device is the atmospheric-pressure plasmas jet (APPJ) [3], which can be operated in different gases and is technologically simple, environmentally-friendly and very economical. The application areas of APPJs include material etching [4], deposition [5], surface modification [6], sterilization [7][8] and in biomedicine such as a wound treatment [7] taking advantage of the very low temperature plasma produced in(to) the ambient air. There are two well known configurations namely the plasma pencil [9] and the plasma needle [10]. Recently, plasma jets, which produce a plasma plume emerging from a fine capillary have been scaled down to produce treatment on the nano-scale (down to tens of nm) [11].

To accompany the technological development, a number of researchers have undertaken advanced diagnostic studies to understand the internal physical and chemical phenomena in APPJs. These include the use of voltage-current probes [12], optical emission spectroscopy (OES) to get gas temperatures [13][14] from emission profile and electron density from Stark broadening [15], 2-D imaging to observe plasma bullet development [16], laser absorption spectroscopy (LAS) [11] and two-photon absorption laser induced fluorescence (TALIF) techniques [17] to determine the density of atoms, Schlieren photograph [18] to observe the invisible gas dynamics and recently molecular beam mass spectrometry [19][20][21][22] [23][24] to determine the ionic composition (both negative and positive ions) from APPJs.

Here we show for the first time the temporal evolution of the mass-selected ionic species in the plasma plume as it interacts with ambient air and correlate the rise and fall of the ionic flux of which the current carried by plasma bullets as they are transported down the plume. In a number of previous mass spectroscopic studies of plasma at atmospheric pressure using an

array for different source configurations (not just the  $\mu$ -APPJ), the emphasis has been on understanding the plasma composition in complex gases or gas mixtures, such air [19],  $\text{N}_2$ - $\text{O}_2$  mixtures [20], He-air [21][22], He- $\text{O}_2$  [23] or He-water mixtures [24] as a feed gas. However, here we concentrate on using a pure He jet and study its interaction with the ambient environment creating secondary ionic species, outside of the main discharge.

## 2. The experimental arrangement

### 2.1 $\mu$ -plasma jet setup

The  $\mu$ -plasma jet used in this study was made using a 15 cm long quartz glass tube of 1 mm inner diameter (ID) and 3 mm outer diameter (OD) on which two copper ring electrodes of 8 mm length were attached as shown in figure 1. The electrode close to the outflow was powered by high ac voltages (6–9 kV,  $V_{p-p}$ ) over a range of frequencies (5–25 kHz). The power supply consisted of a sine wave oscillator (Farnell, LF1) driving a commercial audio amplifier (HQ power, VPA2350MB) with a voltage step-up transformer (Express Transformers, UK) at the output stage to generate the required high voltages for discharge breakdown. The second electrode was electrically grounded. The jet struck in helium gas (99.996 % purity), was operated essentially as a dielectric barrier discharge (DBD), with gas flow rates (between 0.2 and 5.4 L min<sup>-1</sup>), and controlled using a manual rotameter (Omega Engineering). The flexible design allowed the separation and position of the ring electrodes to be changed on the glass tube to aid breakdown and optimise the visible jet length. After preliminary investigations, a gap separation of 25 mm was chosen for all subsequent experiments with a fixed He flow rate of 1.38 slm producing visible plumes of 12 mm in length. To obtain 2-D spatially resolved mass spectroscopic measurements, the  $\mu$ -plasma jet was mounted on an  $x$ - $y$  stage, having a travel range of 20 cm in the axial direction and 12 cm in the radial with 1 mm spatial resolution with the stage placed in front of the mass spectrometer entrance orifice.

### 2.2 Molecular beam mass spectroscopy

The molecular beam mass spectrometer (MBMS) used here was a quadrupole-based mass spectrometer (QMS) system, the HPR-60 MBMS (from Hiden Analytical Ltd.) having a three-stage differentially pumped inlet system separated by aligned skimmer cones and turbo molecular pumps. The pressure reduction stages, ( $P_1$ )–( $P_3$ ) shown in figure 1(a), provide a pressure reduction from atmospheric-pressure to  $10^{-1}$  Torr at the ( $P_1$ ),  $10^{-5}$  Torr at the ( $P_2$ ) and  $10^{-7}$  Torr at the ( $P_3$ ) stage. A molecular beam is formed which is directed into the QMS. Positive and negative ions, generated by the jet (either between the electrodes or through interactions in ambient air) were readily detected, with a mass resolution of 0.01 amu and with an upper mass range of 300 amu. The instrument can also be used in residual gas analyzer (RGA) mode, having an internal ionisation source in the last pressure redactor stage. The mass spectrometer was operated in secondary ion mass spectroscopy (SIMS) mode, with a time resolution of 10  $\mu$ s down to 2  $\mu$ s depending on plasma frequency, obtained by gating the detector using an internal gate signal synchronized to the driving voltage waveform.

The end of the jet capillary was aligned with the centre of the sampling orifice (100  $\mu$ m diameter) and the (nozzle-orifice) distance  $d$  were varied from 1 to 15 mm. Preliminary investigations showed that ionic signals could only be detected with the plasma plume parallel to the axis of the instrument, that is, no ions were detected at radial distances greater than the plume width of 1 mm (close to the spatial resolution of the  $x$ - $y$  stage). The sampling time of the detector was set at 1 s and ions, both positive and negative, of masses between 1 and 100 amu were collected.

To restrict the amount of data in subsequent experiments we chose just three measurement positions in the visible plume, namely at  $d = 1, 7$  and 11 mm, each position showing different interactions of the emerging  $\text{He}^+$  and the ambient air. Three different driving frequencies (5, 10 and 25 kHz) were also used, providing temporal resolutions of 10, 5, and 2  $\mu$ s. Since ions have a significant travel time in the instrument dependent on their mass, to correlate properly the time of their entrance into the instrument and the phase of the voltage cycle, the detection signals were temporally corrected using an algorithm developed at Hiden Analytical Ltd [25].

### 2.3 Discharge and bullet current measurements

To interpret the temporal mass spectroscopic measurements, a correlation to the discharge current and voltage waveforms is necessary. The main discharge current  $I_T$  (flowing between transformer and the driving electrode) was measured using a current probe 1 (Tektronix TCP0030) (see figure 1(b)), with a 120 MHz bandwidth. The electrode voltage was measured with a high voltage probe (HVP-15HF). Both  $V$  and  $I$  were displayed on a digital oscilloscope (DPO3034).  $I_T$  was averaged over 128 cycles, and the large and continuous sinusoidal displacement current  $I_d$  observed in the waveform, (which can be measured without gas flow), was removed from the total signal to give the true discharge current ( $I_D = I_T - I_d$ ).  $I_D$  is composed of the internal discharge current and the free-stream “bullet” current  $I_b$ .

Figure 2 shows waveforms for (a) driving voltage, (b) currents, total  $I_T$  and discharge currents  $I_D$ , and (c) bullet current for a sinusoidal driving voltage 8 kV ( $V_{p-p}$ ) of frequency 10 kHz. The bullet current (described below) was measured 7 mm downstream and the discharge and bullet current peaks coincide in this electrode arrangement because  $I_D$  flow to two pathways, toward the upstream ground electrode and downstream towards the external ground, of roughly equal distance for the driving electrode. The current peaks are several milli-amperes or less, much smaller than the displacement current (few tens mA) as showing in figure 2(b). The width of the current pulse (FWHM) is several micro-seconds. For the bullet current measurements in the outflow, a metal collector plate (copper), connected to the ground line was used and  $I_b$  flowing in this circuit was monitored by the current probe 2. The presence of the metal collector perturbs the free-stream conditions of the plasma plume, however it gives the same electrical conditions as used in the MBMS measurements, where the sampling orifice of the mass spectrometer acted as an external grounded electrode.

#### 2.4 2-D imaging

The visible plasma jet and plasma bullet investigations were carried out using both time-averaged and time-resolved 2-D broadband optical imaging, utilising an ICCD camera (Andor, DH520-18F-01). To determine the total length of the visible plume as shown in figure 3(a) an ICCD exposure time of 0.5 s was used. To resolve individual plasma bullets (known to be present in the plume and correlated to the positive and negative excursions of

the voltage waveform [11][26]) a 100 ns gating time was used, controlled by a trigger pulse (from a Stanford Research Systems, DG645 Digital Delay Generator), synchronized to the driving voltage at time  $t=0$ . The time-resolved image of a single plasma bullet in figure 3(b) was taken at a delay time ( $= 35.6 \mu\text{s}$ ) from which we can distinguish an intense emission head ('bullet head') and a long and faint tail ('bullet halo'). This feature will be discussed later in the context of the MBMS results. The time for the bullet head to pass a fixed point was observed to be few hundred ns but the bullet tail was seen to persist for significantly longer, almost the entire time to the emergence of the next main discharge event. From observation of the bullet head we have calculated the a propagation speed for the bullet of a few tens of kilometre per second, in very good agreement with previous reports [2][16][18]. This is much faster than the gas speed of a few tens metre per second. The current pulse (recorded in the driving circuit corresponding to this bullet) is shown in figure 2(c).

### 3. Results and discussion

#### 3.1 Positive ions

Figure 4(a) and (b) shows the time-averaged mass spectra of positive and negative ions obtained 7 mm from the exit of the capillary along the discharge axis. The excitation voltage was 8 kV at 10 kHz frequency and the flow rate was fixed at  $1.38 \text{ L min}^{-1}$ . The raw mass spectra data has been converted to a relative yield (%)  $Y = Y_i / \sum Y_i$  (%), where  $Y_i$  is the count intensity of a specific species. Ions up to 100 amu have been detected. The positive ion spectra in figure 4(a) reveals singly charged ions, namely  $\text{He}^+$  originating from the primary discharge and another 11 species, created through jet-air interactions. We observed no doubly charges species. These are by % yield, 65.3 % of  $\text{N}_2^+$  and 21.1 % of  $\text{O}_2^+$ , as well as small portions of  $\text{N}^+$ ,  $\text{O}^+$ ,  $\text{N}_2\text{H}^+$ ,  $\text{NO}^+$  and  $\text{Ar}^+$ .  $\text{CO}_2^+$  is also observed but its concentration is less than 0.02 %. The general composition of ions is consistent with those in atmospheric air as shown in table 1.

$\text{He}^+$  ions detected here are created inside the capillary (the primary discharge) via electron-neutral ionization processes in the transverse electric field between electrodes, namely R1)  $\text{e}^-$

1  $+He \rightarrow 2e^- + He^+$  and R2)  $e^- + He_m \rightarrow 2e^- + He^+$ , where  $He_m$  is the  $2^3S$  state metastable helium.  
2 Both  $He^+$  and  $He_m$  species are transported outside the capillary by the mass flow action of the  
3 He gas flowing with a speed of  $30 \text{ m s}^{-1}$ . No helium dimer ions ( $He_2^+$ ) were detected in this  
4 work. This may be due to the measurement only being made outside capillary where charge  
5 transfer between  $He_2^+$  and  $N_2$  and/or  $O_2$  molecules may readily deplete the  $He_2^+$  signal as it  
6 exits the nozzle.

7 A number of secondary positive ion are produced through the interaction of the emerging jet  
8 and ambient air. For instance, molecular nitrogen ions  $N_2^+$  are created by a number of  
9 possible reactions R3)  $He_2^+ + N_2 \rightarrow 2He + N_2^+$  ( $8.3 \times 10^{-10} \text{ cm}^3 \text{ s}^{-1}$ ) [27] and R4)  $He_m + N_2 \rightarrow$   
10  $He + N_2^+ + e^-$  ( $5 \times 10^{-11} \text{ cm}^3 \text{ s}^{-1}$ ) [28], however as we have said no  $He_2^+$  was detected in these  
11 studies and R3) might be unlikely. For  $O_2^+$  production, possible reactions are R5)  $He_m + O_2 \rightarrow$   
12  $He + O_2^+ + e^-$  ( $2.54 \times 10^{-10} \text{ cm}^3 \text{ s}^{-1}$ ), R6)  $He^+ + O_2 \rightarrow He + O_2^+$  ( $3.3 \times 10^{-11} \text{ cm}^3 \text{ s}^{-1}$ ), and R7)  $He^+ + O_2^* \rightarrow$   
13  $He + O_2^+$  ( $3.3 \times 10^{-11} \text{ cm}^3 \text{ s}^{-1}$ ), where  $O_2^*$  is the metastable molecule (state  $^1\Sigma_g^+$ ). The rate  
14 constants R5-R7 have been used in the modelling of both atmospheric pressure [23] and low  
15 pressure plasmas [29]. The reaction rate for the charge transfer from  $He^+$  (or  $He_2^+$ ) and the  
16 ionisation by  $He_m$  to both  $N_2$  and  $O_2$  are similar in order ( $\sim 10^{-11}$  to  $10^{-10} \text{ cm}^3 \text{ s}^{-1}$ ). Therefore,  
17 the positive ion yield should reflect the composition of the ambient air. It therefore stands to  
18 reason that  $N_2^+$  was the highest yield with  $O_2^+$  the second highest.

### 19 3.2 Negative ions

20 For the negative ions, we detected 34 species as shown in figure 4(b). Many of these are  
21 clusters and therefore more massive than the positive ions. It is well known that the negative  
22 ions are produced by the dissociative electron attachment. The main ionic species by relative  
23 abundance are 22.7 % of  $O_3^-$ , 10.5% of  $O_2^-(H_2O)$ , 8.2% of  $OH^-(H_2O)_2$ , 6.4% of  $O_3^-(H_2O)$ ,  
24 5.8% of  $OH^-(H_2O)$ , 5.4% of  $O_2^-$ , 1.9% of  $O^-$ , 0.8% of  $OH^-$  and also clusters,  $O_n^-(H_2O)_m$ ,  
25  $(OH)_n^-(H_2O)_m$ ,  $O_n^-(CO_3)$ ,  $CO_3^-(H_2O)_n$ , and so on. Table 1 provides the complete set of  
26 species with relative percentage yields, showings that clusters dominate the spectrum of  
27 negative ions. This is because not only do negative ions form through dissociative electron

attachment ( $e+AB \rightarrow A^-+B$ ) [24] but the product ions readily undergo further attachment processes ( $A^-+M \rightarrow A^-M$ ), where M denotes molecules in air, to form heavier species.

The dissociative electron attachment of  $H_2O$  and subsequently hydration has been reported for negative ion formation in Ref. [24] where a He-water mixture was used to produce moist gas, then fed into a glow discharge in an isolated space (not exposure to air). In our work, however, the most intense peaks of negative ions are oxygen molecules such as  $O_3^-$ ,  $O_2^-$  ( $H_2O$ ) and  $O_3^-(H_2O)$ , indicating the main pathway of creation is through dissociative electron attachment of  $O_2$  and subsequent oxidation to form many of the negative ion species. From the data in table 1 we also see the overall yield for oxygen containing molecule ions ( $O_n^-$ ) is 45%, while the overall yield for hydroxyl ( $OH$ ) $_n^-$  containing ions is 25%. This indicates that here atmospheric molecular oxygen is more important than water vapour in the production of negative ions. To illustrate this, to produce  $O_3^-$ , we can consider two possible routes, the dissociative electron attachment of both  $O_2$  and water, R8)  $e^-+2O_2 \rightarrow O^-+O+O_2$  and R9)  $e^-+H_2O+O_2 \rightarrow O^-+H_2+O_2$ , followed by attachment R10)  $O^-+O+O_2 \rightarrow O_3^-+O$ . R8 and R9 reactions have similar cross sections for dissociative electron attachment [30][31]. Since the concentration atmospheric  $O_2$  is at least 50 times greater than that of water molecules in the air, even in humid conditions, the main reaction route for formation of  $O_3^-$  is a series of R8 and R10. Our observations of a high content of species like  $O_3^-$  and  $O_2^-(H_2O)$ , and few species such as  $OH^-(H_2O)$  as also found in [24] is due to the presence of atmospheric oxygen (contained in moisture free) which become mixed or entrained in the He gas flow.

Since the positive and negative ions are formed through wholly different processes it is expected that each process may be separated spatially and temporally. To understand better the processes leading to ionic formation, time-resolved mass spectroscopy has been carried out at a number of locations along the visible glow and the results are discussed in section 3.4 below.

### 3.3 Spatial distribution of ionic concentrations

Figure 5(a) and (b) shows the relative concentration of selected positive and negative ions detected along the length of the plasma plume, from 1 mm from exit of the capillary to a

1 maximum distance of 15 mm. The ions can be detected inside of the visible plume and up to  
2 a more few mm outside the plume along the axis, a region characterised by laminar (non-  
3 turbulent flow) He gas flow [18][32]. One should note that the mass spectrometer flange  
4 containing the sampling orifice can act as an external electrode (being grounded) and so  
5 changing the mass-spectrometer capillary distance will affect the discharge. The visible  
6 extension of the plume (viewed by eye and ICCD camera) was measured to around 12 mm.  
7 See the image in figure 3(a).

8 The positive and negative ion species show some differences in behaviour. For the positive  
9 ions in figure 5(a), we see the  $\text{He}^+$ ,  $\text{N}_2^+$  and  $\text{O}_2^+$  concentrations remains high up to a distance  
10 of 6 mm, after which there is peak of width 3 mm followed by a drop of 4 orders of  
11 magnitude to no discernable signal between 14 and 15 mm. The peak intensity midway along  
12 the plume coincided with a very strong rise in  $\text{NO}^+$ , and also  $\text{N}_2^+$  and  $\text{O}_2^+$  intensities between  
13 7 and 11 mm. In this region there must be strong mixing of air with jet exhaust. The negative  
14 ion concentrations in figure 5(b) show no outstanding strong peak midway along the plume  
15 but there is gradual rise in the heavy  $\text{O}_3^-$  signal beginning at 7 mm where the positive ions  
16 intensities increase. The intensities remain constant before falling rapidly beginning at 12 mm,  
17 which corresponds to the tip of visible plume, as shown in figure 3(a). The light species such  
18 as atomic  $\text{O}^-$  are terminated more quickly than the heavier species such as  $\text{O}_3^-$ . The velocities  
19 of the ions may be mass dependent; however we have no information on the energy of the  
20 ions in the plasma plume. Clearly comparing positive and negative ions in figure 5(a) and (b)  
21 we see the negative ions extend further past the end of the visible plume than the positive  
22 species, being still detectable at 15 mm.

### 23 3.4 Time-resolved SIMS, 2-D imaging and current measurements

24 Since the first work conducted in the group of Engemann [16] it has been shown many times  
25 that the visible plasma emission extending from the DBD micro-jet propagates at very fast  
26 speeds (up to  $\sim 10^2 \text{ km s}^{-1}$ ) in the form of discrete packets referred to as plasma “bullets”.  
27 Recently, it is also reported that for ac driven APPJs, bullets have their origin when the  
28 driving voltage reaches a threshold in the positive and negative going parts of the voltage

cycle [26]. In brief, the plasma bullet triggered from positive half period shows an intense and bright emission. While negative half period bullet is observed faint and broad. However, initiation of both is localised around few mm and can be clearly observed only within duration of a few microseconds after initiation.

The ionic content of the bullet (its head and following tail or halo) has not yet been determined. Here, through time-resolved measurements ( $\text{He}^+$  and secondary positive and negative) ions we can correlate the time over which ionic species rise, persist and subsequently fall during the voltage cycle to the time the bullet of length  $\sim 12$  mm (consisting of head and tail) passes a point in space.

For the time-resolved MBMS studies, the mass selected ion concentrations were measured at three distances 1, 7 and 11 mm from the exit orifice of the capillary over two whole periods of the driving voltage (e.g. this is  $400\ \mu\text{s}$  when operating at 5 kHz). The time-resolution of the ionic concentrations (both positive and negative) changed depending on the driving frequency, i.e.  $10\ \mu\text{s}$  at 5 kHz and  $2\ \mu\text{s}$  at 25 kHz. To aid interpretation, we have chosen to display a 6 positive species ( $\text{O}_2^+$ ,  $\text{O}^+$ ,  $\text{N}_2^+$ ,  $\text{N}^+$ ,  $\text{He}^+$  and  $\text{Ar}^+$ ) and 6 negative species ( $\text{O}^-$ ,  $\text{OH}^-$ ,  $\text{O}_3^-$ ,  $\text{OH}^-(\text{H}_2\text{O})$  and  $\text{H}_2\text{O}^-$ ), having a behaviour and response representative of all the ions detected as listed in table 1 and shown in figure 4.

#### 3.4.1 Effect of distance

Figure 6 to 8 shows the temporal evolution of the ionic species together in each figure with the driving voltage waveform, the discharge current  $I_D$  and local bullet current  $I_b$  measurements. The relative concentrations of the positive and negative species reflect the time-average mass spectra in figure 4 with the most intense species being  $\text{N}_2^+$  and  $\text{O}_2^+$  for the positive ions  $\text{O}_3^-$  and  $\text{O}^-$  for the negative ions. The magnitude of the positive and negative local bullet currents  $I_b$  follow those of the general ionic intensity, i.e. small currents are associated with small ionic intensities. So we can see the passing bullet delivers positive ionic species to the instrument in each voltage half cycle.

All the three figures 6-8, show the same strong features. In the positive voltage half cycle with an associated positive discharge current pulse (and directly correlated with the start of

the local bullet current) we observe a sharp rise in the positive ion concentration (by 3 orders of magnitude) within about 10  $\mu$ s. When two current peaks appear, in either of the positive or negative parts of the voltage cycle, as seen clearly in figure 6, we also observe two peaks in the positive ion intensities, correlated directly to the features in the current. Fast positive ion rise times may be due to rapid electron induced collisional ionisation with ions and neutrals. The electrons will be streaming in the direction from the external ground toward the positive electrode on the capillary. This is sustained for about 50  $\mu$ s after which the ionic intensities fall all at similar rates. Interestingly, we also observe a clear and rapid rise in the positive ionic intensities on the negative voltage half cycle correlated to the negative discharge current (and local bullet current measurement). The positive ion intensities are however clearly weaker in this part of the voltage cycle. This may be due to the reduction in the ionisation rate of neutrals to form positive ions via electron collisions in this part of the cycle as the electrons are readily attached in great numbers to form negative ions.

For the case of the negative ions, their rise is correlated to the negative part of the voltage cycle, reaching their peak on fast time-scales ( $\sim 10$   $\mu$ s) similar to the positive ions, but they persist for much longer sustaining times up to 100-150  $\mu$ s, displaying much slow decays, and showing little response to the subsequent positive voltage half cycle. The correlation of negative ions with negative voltage swings on the powered electrode may be associated with the axial electric field which will act to accelerate electrons out into the plume, where they readily attach to molecules in dissociative reactions to form families of negative ions. In the positive half cycle the concentration of electrons in the plume may be reduced as the powered electrodes acts as an effective electron sink.

The negative ions, with decay time constants  $\tau \sim 20$   $\mu$ s display a modulation once every cycle rather than a twice as with the positive ions. We may be able to understand that heavier species, such as negative ion clusters will have lower mobilities and longer lifetimes in air than the lighter positive ions [23], however here  $O^-$  displays decay times many times longer than  $O^+$  (see figure 6 to 8). It is reported that ions such as  $OH^-$  can have lifetime of 1 ms

being stable in air [33] however primary ions in reactions such as  $O^-$  have shorter lifetimes and short mean free paths of about  $0.1\ \mu\text{m}$ .

Close inspection of the figure 6 to 8 shows there is some small modulation of the measured intensities of the lighter ions  $O^-$ ,  $H^-$  and  $OH^-$  in the positive half cycle of the voltage. With increasing distances, it is clear that atomic  $O^-$  flux is reduced. The fluxes of heavy molecules,  $O_3^-$  and  $OH(H_2O)$ , are maximised at the 7 mm where a strong interaction between plasma jet and surrounding air is expected as mention above subsection 3.3.

The amount of mixing of the air with the He stream will be an important factor in determining the amount of negative ionic species (clusters) detected in the plume created through reactions R8 and R9, and then by further oxidisation and/or hydration processes.

It is clear in figure 6 to 8 that both the discharge current and the locally measured current in the plume (bullet current) consist of a rapid pulse of width of only several microseconds; however the peaks ionic spectra last much longer ( $\sim 50\ \mu\text{s}$  and  $\sim 100\ \mu\text{s}$  for the positive and negative ions respectively).

Inspection of the bullet current waveforms (for example that in figure 2(c)), shows the head contains most of the total charge associated with bullet with about 25 % contained in the long tail. For positive currents the head contains positive ions and few negative ions ( $<10\%$ ) which are decaying in density from the previous pulse. The duration of tail which also consists mostly of positive ions passing any point coincide with the duration of the positive ionic signals in mass spectroscopic results. For negative going bullet currents the head contains a high proportion of negative ions and some positive ions (as shown in mass spectroscopic results in figure 6). In this case, the bullet tail contains negative ionic species.

### 3.4.2 Ionic life-times

For bullet formation outside the capillary, we see a bright head of length typically 2-3 mm followed by a visually weaker but attached tail. As the head advances (with velocities up to  $23\ \text{km s}^{-1}$  measured using the ICCD camera), the tail elongates, being essentially clamped to the end of the capillary for at least  $10\ \mu\text{s}$  observed before the next main discharge event, see also [2][16][34][35][36][37]. Even when the bullet is terminated at the external grounded

electrode (or current collector), the bullet tail persists for some time. In free stream conditions, it has been observed that after about several  $\mu\text{s}$  the bullet head dissipates, as the mole fraction of He gas in ambient air falls below a critical value as turbulence sets in to the flow [18].

The results from the time-resolved mass spectrometric measurements here show remarkably long times for the existence of both positive and negative species, between  $\sim 50$  and  $\sim 150 \mu\text{s}$  respectively. This time-scale is much longer than the time the bullet traverses between the capillary end and the mass spectrometer orifice, and longer than the time we observe the optical emission from the long bullet tail. However, although the tail is not observed some  $50 \mu\text{s}$  after the bullet initiation we argue that the passing bullet has created a halo of secondary positive and negative ions which have significant life-times. The fast increase in ionic signal for both polarity ions ( $10 \mu\text{s}$  rise time), correlated with the local bullet current measurement is characteristic of the creation of species as electrons (or possibly  $\text{He}^+$ ) ions rapidly pass through the gas. Once created, the negative ions (including heavy clusters) have longer lifetimes than the positive species, possibly due to higher ionic stabilities, more complex destruction reaction routes or lower ion mobilities in the ambient air [33][38]. The distance over which ions travel to the mass spectrometer from their point of creation can be determined, from knowledge of the lifetimes and the speed of the gas that transports them downstream. Here we have a He gas speed of  $30 \text{ ms}^{-1}$  and assuming  $50\text{-}100 \mu\text{s}$  lifetimes it gives a distance of about  $1.5$  to  $3 \text{ mm}$ . It seems likely therefore that the detected species both positive and negative ions have been created close to the spectrometer orifice, however coming from distance much greater than reported elsewhere [38] and this we cannot explain with the limited data of this study.

### *3.4.3 Effect of driving frequency*

The ionic intensities measured for pulse frequencies of  $10$  and  $25 \text{ kHz}$  are shown in figures 9 and 10 respectively. It is clear that the peak ionic fluxes are reduced at higher frequencies. Also, we see only one current peak per half cycle of the discharge voltage. These observations are not understood but will be explored in further studies. At  $25 \text{ kHz}$  the negative ions respond less well to the voltage modulation, however the positive ions intensities

still show a clear time modulation, with 10  $\mu$ s rise and decay times similar to those in figures 6-8 for a 5 kHz frequency. The  $N_2^+$  and  $O_2^+$  signals rise and fall as before at other frequencies but atomic ions,  $N^+$  and  $O^+$ , are delayed around 10  $\mu$ s relative to these, this may be due to the stepwise process necessary to produce atomic ions from air species. For the negative ions, at 10 and 25 kHz the atomic  $O^-$  and  $OH^-$  molecule intensities are measured in advance of the heavier ions such as  $O_3^-$ ,  $O_2^-(H_2O)$ ,  $OH^-(H_2O)_2$ ,  $O_3^-(H_2O)$  and  $OH^-(H_2O)$ , this may also be due to multi-step processes necessary for their creation and possibly longer travel times from the point creation to the mass spectrometer orifice.

Although we see almost a flat response in the negative ion signal at 25 kHz, inspection of the curves on a linear scale reveal the same rise and decay time constant as for 5 and 10 kHz. At 25 kHz, half the period is 20  $\mu$ s, close to the decay time constant for the negative ions; hence it is possible that an equilibrium concentration along the plume of negative ions may develop with only a small modulation in intensities during the voltage cycle, as can be seen in figure 10.

#### 4. Conclusions

Using time-resolved molecular beam mass spectrometry negative and positive ions have been detected in the output plume of an atmospheric pressure plasma micro-jet operating in He at 5-25kHz. The results show that positive ions (for instance  $He^+$ ,  $N_2^+$  and  $O_2^+$ ) are created on the positive and negative voltage swings and persist for about 50  $\mu$ s. The creation of negative ions (e.g.  $O_3^-$ ,  $O_2^-(H_2O)$ ,  $OH^-(H_2O)_2$ ,  $O_3^-(H_2O)$ ,  $OH^-(H_2O)$  and clusters) is correlated however only to the negative part of the voltage cycle, but these species have very long decay times (3 or 4 times longer for the full decay than the positive ions). The ionic components are only observed in the visible plasma plume and up to 1 to 2 mm distance beyond its end.

The temporal increase of the signal of both positive and negative ionic species in the mass spectra is correlated directly with the rise of the discharge and local bullet currents. The current from the head of individual bullets only exists for several microseconds, much shorter

1 than the detected time of the ionic species (50 to 150  $\mu$ s). As the bullet head passes through  
2 the neutral (non-turbulent) He stream, it produces a halo of secondary ions of both polarities.  
3 Inspection of the bullet current waveforms together with time-resolved optical imaging and  
4 mass spectroscopic results indicates that the bright head of the bullet contains most of the net  
5 space charge, with the faint bullet tail (halo) of lower space charge persisting for long times  
6 over which the ionic species are detected. At highest frequency of 25 kHz, when half the  
7 driving period becomes close to the characteristic decay time of the negative ions a constant  
8 (almost equilibrium) concentration of negative ions can be maintained adjacent to the orifice  
9 of the mass spectrometer.

#### 11 **Acknowledgement**

12 We thank Mr. Alan Roby for the construction of the microplasma jet rig. This work was  
13 supported by the Engineering and Physical Sciences Research Council (EPSRC) grant  
14 reference: EP/G048444/1.

## Figure captions

**FIG. 1** (a) showing schematic of the experimental setup, the HPR-60 molecular beam mass spectrometer with an atmospheric pressure micro-plasma jet on the  $x$ - $y$  stage placed in front of the 100  $\mu\text{m}$  orifice. P1, P2, and P3 are pressure reduction stages. (b) shows a schematic of voltage and current measurements.

**FIG. 2** Plots of the typical driving voltage (a), current signals, total and discharge currents, (b) and bullet current (c). In this case the driving frequency is 10 kHz.

**FIG. 3** An image of a plasma jet driven 10 kHz and 8  $\text{kV}_{\text{p-p}}$  ac, and 1.38 slm helium flow taken using an ICCD camera. (a) shows time-averaged plasma plume (0.5 s exposure time) and (b) shows time-averaged plasma bullet (100 ns exposure time and 35.6  $\mu\text{s}$  delay time).

**FIG. 4** A mass spectra plot of positive ions (a) and negative ions (b), measured in the outflow plasma jet at a distance of 7 mm from the gas nozzle. The jet was operated at 10 kHz and 8  $\text{kV}_{\text{p-p}}$  ac, with 1.38 slm helium flow.

**FIG. 5** The spatial distributions of (a) positive ion flux and (b) negative ion flux along a line between the jet nozzle and the instrument orifice. The same operating conditions as in fig 4.

**FIG. 6** The time-resolved positive and negative ion fluxes for selected species measured 1 mm from the nozzle at 5 kHz. The associated voltage, discharge and bullet currents are also shown.

**FIG. 7** The time-resolved positive and negative ion fluxes for selected species measured 7 mm from the nozzle at 5 kHz. The associated voltage, discharge and bullet currents are also shown.

**FIG. 8** The time-resolved positive and negative ion fluxes for selected species measured 11 mm from the nozzle at 5 kHz. The associated voltage, discharge and bullet currents are also shown.

**FIG. 9** The time-resolved positive and negative ion fluxes for selected species measured 7 mm from the nozzle at 10 kHz. The associated voltage, discharge and bullet currents are also shown.

**FIG. 10** The time-resolved positive and negative ion fluxes for selected species measured 7 mm from the nozzle at 25 kHz. The associated voltage, discharge and bullet currents are also shown.

**Table 1** The positive and negative species detected in the plasma plume with their relative abundance by atomic percentage.

amu	Standard atmosphere	Micro-plasma jet and ambient air	
	Neutrals	Positive ions	Negative ions
4		He <sup>+</sup> (1.79)	
14		N <sup>+</sup> (2.38)	
16		O <sup>+</sup> (2.48)	O <sup>-</sup> (1.89)
17			OH <sup>-</sup> (0.76)
18	H <sub>2</sub> O (0.4)	H <sub>2</sub> O <sup>+</sup> (0.37)	
28	N <sub>2</sub> (78.08)	N <sub>2</sub> <sup>+</sup> (65.26)	
29		N <sub>2</sub> H <sup>+</sup> (1.38)	
30		NO <sup>+</sup> (3.76)	
32	O <sub>2</sub> (20.94)	O <sub>2</sub> <sup>+</sup> (21.11)	O <sub>2</sub> <sup>-</sup> (5.43)
33		(OH)O <sup>+</sup> (0.15)	(OH)O <sup>-</sup> (2.68)
34		O(H <sub>2</sub> O) <sup>+</sup> (0.12)	O <sup>-</sup> (H <sub>2</sub> O) (1.19)
35			OH <sup>-</sup> (H <sub>2</sub> O) (5.79)
40	Ar (0.9337)	Ar <sup>+</sup> (0.56)	
44	CO <sub>2</sub> (0.039)		
46			NO <sub>2</sub> <sup>-</sup> (0.79)
48			O <sub>3</sub> <sup>-</sup> (22.68)
50			O <sub>2</sub> <sup>-</sup> (H <sub>2</sub> O) (10.49)
51			(OH)O <sup>-</sup> (H <sub>2</sub> O) (3.80)
52			O <sup>-</sup> (H <sub>2</sub> O) <sub>2</sub> (0.46)
53			OH <sup>-</sup> (H <sub>2</sub> O) <sub>2</sub> (8.19)
60			CO <sub>3</sub> <sup>-</sup> (3.60)
61			HCO <sub>3</sub> <sup>-</sup> (3.25)
62			NO <sub>3</sub> <sup>-</sup> (0.36)
65			O <sub>3</sub> (OH) <sup>-</sup> (2.18)
66			O <sub>3</sub> <sup>-</sup> (H <sub>2</sub> O) (6.44)
67			O(OH) <sub>3</sub> <sup>-</sup> (0.34)
68			O <sub>2</sub> <sup>-</sup> (H <sub>2</sub> O) <sub>2</sub> (1.78)
69			(OH)O <sup>-</sup> (H <sub>2</sub> O) <sub>2</sub> (1.46)
71			OH <sup>-</sup> (H <sub>2</sub> O) <sub>3</sub> (2.08)
76			O(CO <sub>3</sub> ) <sup>-</sup> (0.20)
77			OH(CO <sub>3</sub> ) <sup>-</sup> (3.77)
78			CO <sub>3</sub> <sup>-</sup> (H <sub>2</sub> O) (0.27)
79			HCO <sub>3</sub> <sup>-</sup> (H <sub>2</sub> O) (1.41)
82			NO <sub>2</sub> <sup>-</sup> (H <sub>2</sub> O) <sub>2</sub> (0.30)
84	Kr (0.65E-4)		O <sub>3</sub> <sup>-</sup> (H <sub>2</sub> O) <sub>2</sub> (0.96)
86			O <sub>2</sub> <sup>-</sup> (H <sub>2</sub> O) <sub>3</sub> (0.27)
87			(OH)O <sup>-</sup> (H <sub>2</sub> O) <sub>3</sub> (0.85)
89			OH <sup>-</sup> (H <sub>2</sub> O) <sub>4</sub> (1.25)
94			NO <sub>5</sub> <sup>-</sup> (1.36)
95			(OH)CO <sub>3</sub> <sup>-</sup> (H <sub>2</sub> O) (1.42)
96			CO <sub>3</sub> <sup>-</sup> (H <sub>2</sub> O) <sub>2</sub> (0.23)
97			HCO <sub>3</sub> <sup>-</sup> (H <sub>2</sub> O) <sub>2</sub> (0.89)

---

## References

- [1] Liston E M, Martinu L and Wertheimer M R 1994 Plasma surface modification of polymers: relevance to adhesion *VSP BV Chapter 1*
- [2] Tachibana K 2006 Current status of microplasma research *IEEJ Trans.* **1** 145-155
- [3] Koinuma H, Ohkubo H, Hashimoto T, Inomata Kiyoto, Shiraishi T, Miyanaga A, Hayashi S 1991 Development and application of a microbeam plasma generator *Applied Physics Letter*, **60** 816
- [4] Jeong J Y, Babayan S E, Tu V J, Park J, Henins I, Hicks R F and Selwyn G S 1998 Etching materials with an atmospheric-pressure plasma jet *Plasma Sources Sci. Technol.* **7** 282
- [5] Ito Y, Urabe K, Takano N, Tachibana K 2008 High speed deposition of SiO<sub>2</sub> films with plasma jet based on capillary dielectric barrier discharge at atmospheric pressure *Appl. Phys. Express*, **1** 067009-3
- [6] Szili E J, Al-Baraineh A S, Bryant P M, Short R D, Bradley J W, and Steele D A 2011 Controlling the spatial distribution of polymer surface treatment using atmospheric-pressure microplasma jets *Plasma Process. Polym.* **8** 38
- [7] Lee K, Paek K-H, Ju W-T and Lee Y 2006 Sterilization of bacteria, yeast, and bacterial endospores by atmospheric-pressure cold plasma using helium and oxygen *Journal of Microbiology* **44** 269-275
- [8] Fridman G, Friedman G, Gutsol A, Shekhter A B, Vasilets V N and Fridman A 2008 Applied plasma medicine *Plasma Process. Polym.* **5** 503-533
- [9] Price R O, Chiavanini R, Kolb J F and Schoanbach K H 2009 Cold air atmospheric pressure micro plasma jet application method and device *United States Patent* US2009/0121638A1
- [10] Stoffels E, Flikweert A J, Stoffels W W and Kroesen G M W 2002 Plasma needle: a non-destructive atmospheric plasma source for fine surface treatment of (bio)materials *Plasma Sources Sci. Technol.* **11** 383

- 
- [11] Kakei R, Ogino A, Iwata F and Nagatsu M 2010 Production of Ultrafine Atmospheric Pressure Plasma Jet with Nano-capillary *Thin Solid Films* **518** 3457
- [12] Urabe K, Morita T, Tachibana K and Ganguly B N 2010 Investigation of discharge mechanisms in helium plasma jet at atmospheric pressure by laser spectroscopic measurements *J. Phys. D: Appl. Phys.* **43** 095201
- [13] Walsh J L, Shi J J and Kong M G 2006 Contrasting characteristics of pulsed and sinusoidal cold atmospheric plasma jets *Appl. Phys. Lett.* **88** 171501
- [14] Bruggeman P, Iza F, Guns, Lauwers D, Kong M G, Aranda Gonzalvo Y, Leys C and Schram D C 2010 Electronic quenching of OH(A) by water in atmospheric pressure plasmas and its influence on the gas temperature determination by OH(A-X) emission *Plasma Sources Sci. Technol.* **19** 015016
- [15] Qian M, Ren C, Wang D, Zhang J and Wei G 2010 Stark broadening measurement of the electron density in an atmospheric pressure argon plasma jet with double-power electrodes *J. Appl. Phys.* **107** 063303
- [16] Teschke M, Kedzierski J, Finantu-Dinu E G, Korzec D and Engemann J 2005 High-speed photographs of a dielectric barrier atmospheric pressure plasma jet *IEEE Tran. on Plasma Sci.* **33** 310
- [17] Mazouffre S, Bakker I, Vankan P, Engeln R and Schram D C 2002 Tow-photon laser induced fluorescence spectroscopy performed on free nitrogen plasma jets *Plasma Sources Sci. Technol.* **11** 439
- [18] Oh J-S, Olabanji O T, Hale C, Mariani R, Kontis K and Bradley J W 2011 Imaging gas and plasma interaction in the surface chemical modification of polymers by micro-plasma jet *J. Phys. D: Appl. Phys.* **44** 155206
- [19] Skalny J D, Orszagh J, Mason N J, Rees J A, Aranda-Gonzalvo Y and Whitmore T D 2008 Mass spectrometric study of negative ions extracted from point to plane negative corona discharge in ambient air at atmospheric pressure *Intl. J. Mass Spectrometry* **272** 12

- 
- [20] Malović G, Puač N, Laszović S and Petrović Z 2010 Mass analysis of an atmospheric pressure plasma needle discharge *Plasma Sources Sci. Technol.* **19** 034014
- [21] Stoffels E, Aranda-Gonzalvo Y, Whitmore T D, Seymour D L and Rees J A 2007 Mass spectrometric detection of short-living radicals produced by a plasma needle *Plasma Sources Sci. Technol.* **16** 549
- [22] Rees J A, Seymour D L, Greenwood C-L, Aranda-Gonzalvo Y and Lundie D T 2008 Mass and energy spectrometry of atmospheric pressure plasmas *Plasma Process. Polym.* **7** 92
- [23] Waskoenig J, Niemi K, Knake N, Graham L M, Reuter S, Schulz-von der Gathen V and Gans T 2010 Atomic oxygen formation in a radio-frequency driven micro-atmospheric pressure plasma jet *Plasma Sources Sci. Technol.* **19** 045018
- [24] Bruggeman P, Iza F, Lauwers D and Aranda-Gonzalvo Y 2010 Mass spectrometry study of positive and negative ions in a capacitively coupled atmospheric pressure RF excited glow discharge in He-water mixtures *J. Phys. D: Appl. Phys.* **43** 012003
- [25] Probe transit time <http://www.hiddenanalytical.com/>
- [26] Oh J-S, Bryant P M and Bradley J W 2010 Discharge and Plasma Bullet Formation in a Capillary DBD Atmospheric Pressure Micro-plasma Jet *IEEE Tran. on Plasma Sci.* in press.
- [27] Pouvesle J M, Bouchoule A and Stevefelt J 1982 Modelling of the charge transfer afterglow by intense electrical discharges in high pressure helium nitrogen mixtures *J. Chem. Phys.* **77** 817
- [28] Martens T, Bogaerts A, Brok W J M and Dijk J V 2008 The dominant role of impurities in the composition of high pressure noble gas plasmas *Appl. Phys. Lett.* **92** 041504
- [29] Stafford D S and Kushner M J 2004 O<sub>2</sub> (<sup>1</sup>Δ) production in He/O<sub>2</sub> mixtures in flowing low pressure plasmas *J. Appl. Phys.* **96** 2451
- [30] Itikawa Y 2009 Cross sections for electron collisions with oxygen molecules *J. Phys. Chem. Ref. Data* **38** 1

- 
- [31] Itikawa Y and Mason N 2005 Cross sections for electron collisions with water molecules *J. Phys. Chem. Ref. Data* **34** 1
- [32] Karakas E, Koklu M and Laroussi M 2010 Correlation between helium mole fraction and plasma bullet propagation in low temperature plasma jets *J. Phys. D: Appl. Phys.* **43** 155202
- [33] Sekimoto K and Takayama M 2010 Negative ion formation and evolution in atmospheric pressure corona discharges between point-to-plane electrodes with arbitrary needle angle *Eur. Phys. J. D* **60** 589-599
- [34] Walsh J L and Kong M G 2008 Frequency effects of plasma bullets in atmospheric glow discharges *IEEE Trans. on Plasma Sci.* **36** 954
- [35] Sands B L, Ganguly B N and Tachibana K 2008 A streamer-like atmospheric pressure plasma jet *Appl. Phys. Lett.* **92** 151503
- [36] Laroussi M, Hynes W, Akan T, Lu X and Tendero C 2008 The plasma pencil: a source of hypersonic cold plasma bullets for biomedical applications *IEEE Trans. on Plasma Sci.* **36** 1298
- [37] Cao Z, Walsh J L and Kong M G 2009 Atmospheric plasma jet array in parallel electric and gas flow fields for three-dimensional surface treatment *Appl. Phys. Lett.* **94** 021501
- [38] Sabo M, Páleník J, Kučera M, Han H, Wang H, Chu Y and Matejčík S 2010 Atmospheric pressure corona discharge ionisation and ion mobility spectrometry/mass spectrometry study of the negative corona discharge in high purity oxygen and oxygen/nitrogen mixtures *Intl. J. Mass Spectrometry* **293** 23-27,

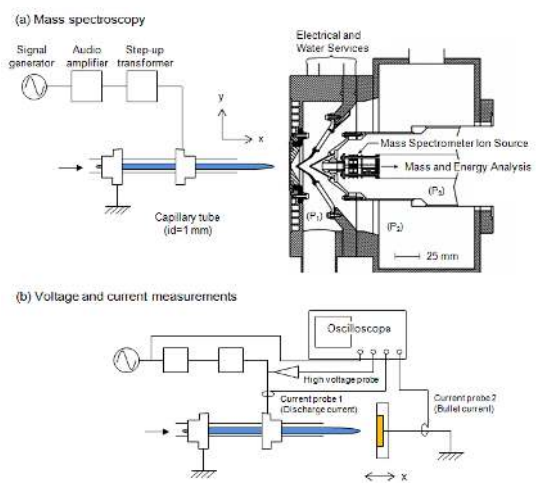
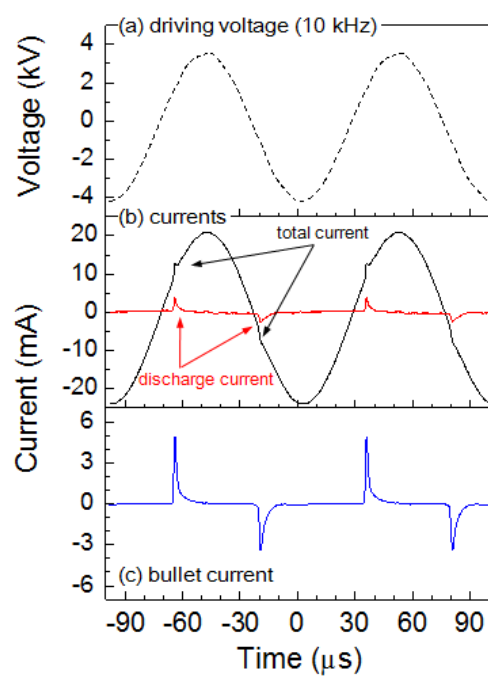
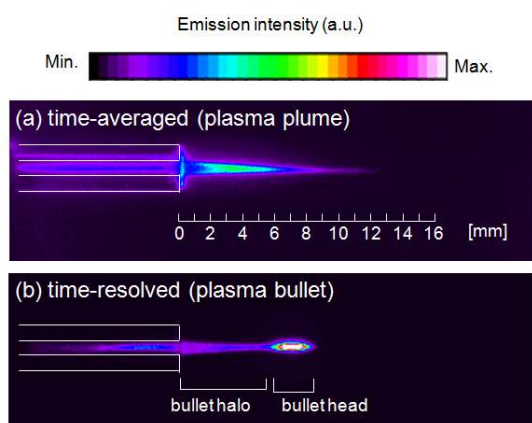


Figure 1 (Fig 1 R1.bmp)



**Figure 2 (Fig 2 R1.bmp)**



**Figure 3 (Fig 3 R1.bmp)**

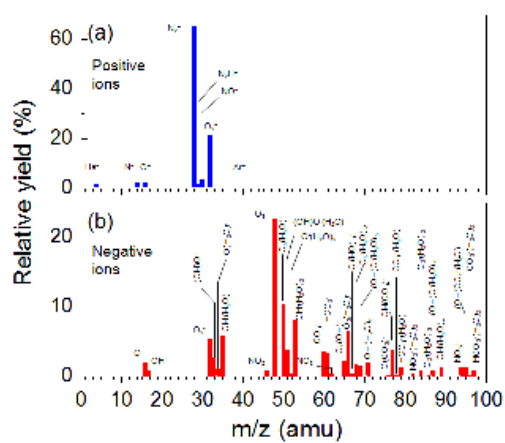


**Figure 4 (Fig 4 R1.bmp)**

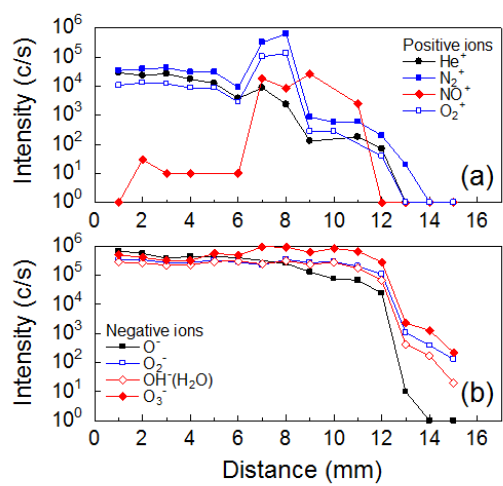


**Figure 5 (Fig 5 R1.bmp)**

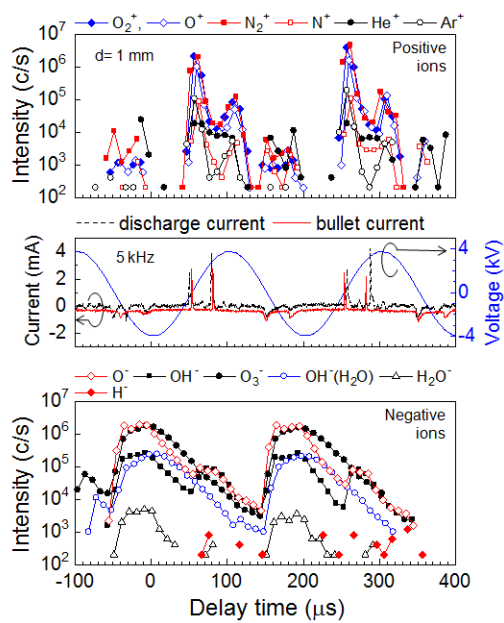


Figure 6 (Fig 6 R1.bmp)

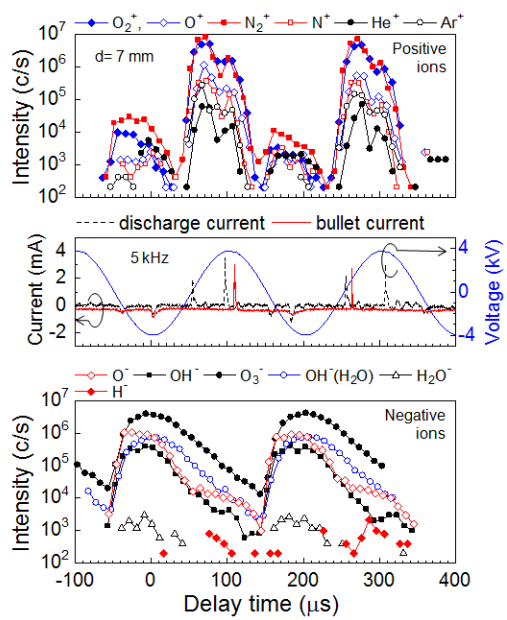


Figure 7 (Fig 7 R1.bmp)

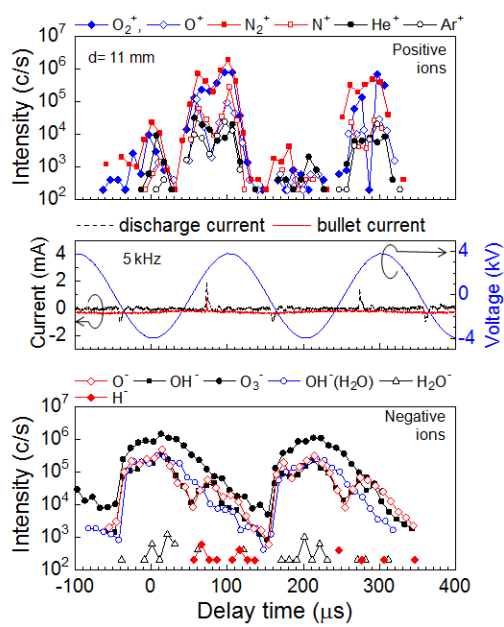


Figure 8 (Fig 8 R1.bmp)

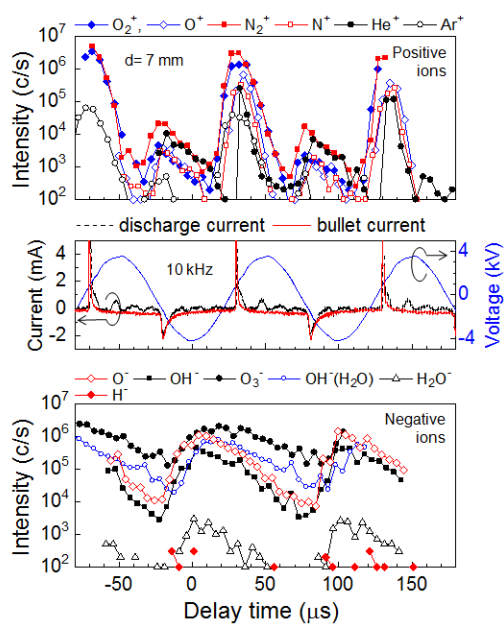
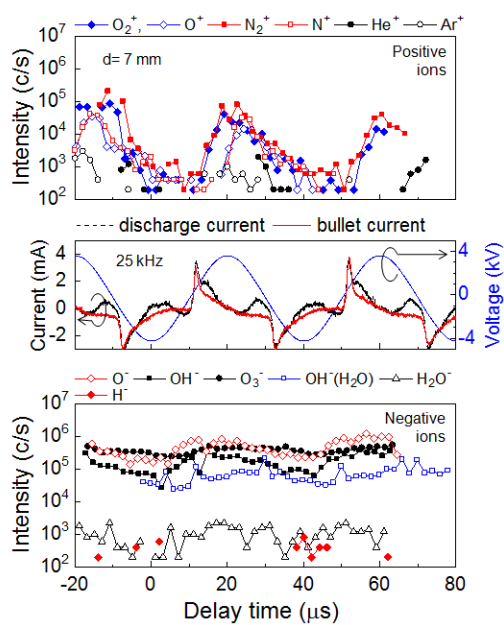


Figure 9 (Fig 9 R1.bmp)



**Figure 10 (Fig 10 R1.bmp)**